Hyperspectral interferometry for single-shot absolute measurement of two-dimensional optical path distributions

J. M. Huntley, T. Widjanarko, and P. D. Ruiz

Loughborough University,
Department of Mechanical Engineering,
Loughborough LE11 3TU, UK

E-mail J.M.Huntley@lboro.ac.uk

Abstract.

We propose a method that we call Hyperspectral Interferometry (HSI) to resolve the 2π phase unwrapping problem in the analysis of interferograms recorded with a narrow-band light source. By using a broad-band light source and hyperspectral imaging system, a set of interferograms at different wavenumbers are recorded simultaneously on a high resolution image sensor. These are then assembled to form a three-dimensional intensity distribution. By Fourier transformation along the wavenumber axis, an absolute optical path difference is obtained for each pixel independently of the other pixels in the field of view. As a result, interferograms with spatially distinct regions are analysed as easily as continuous ones. The approach is illustrated with a HSI system to measure 3-D profiles of optically smooth or rough surfaces. Compared to existing profilometers able to measure absolute path differences, the single shot nature of the approach provides greater immunity from environmental disturbance.

PACS codes: 07.60.Ly, 42.30.Rx, 42.30.Wb, 42.87.Bg

Keywords: Interferometry, Phase Unwrapping, Shape Measurement, Profilometry, Absolute Distance Measurement, Optical Coherence Tomography

1 Introduction

Interferometry is a well-established optical technique for measuring distances between an object and a reference surface to an accuracy of a small fraction of the wavelength of light. Although sometimes used in a pointwise or linewise configuration, it is at its most powerful when used to provide two-dimensional information. Examples of commercial applications include optical component testing, displacement field measurement using speckle interferometry, and profilometry of small scale mechanical and electronic devices using scanning white light interferometry.

In its standard forms, interferometry can suffer from some drawbacks related firstly to the uniqueness of the measured optical path length data, and secondly to the sensitivity of the technique to environmental disturbances. In the current paper we propose a generic form of 2-D interferometer based on simultaneous illumination of the sample with light of multiple wavelengths, and subsequent separation of the different wavelength bands using a hyperspectral imaging system. The multiple wavelength approach solves the uniqueness problem, and the simultaneous illumination provides a single shot capability that can practically eliminate the influence of environmental disturbance.

We describe in more detail the problems of conventional single-wavelength interferometry in Section 2, before outlining the concept of hyperspectral interferometry (HSI) in Section 3. Finally, an example of such a hyperspectral interferometer for measuring 3-D surface profiles is described in Section 4.

2 Some problems with conventional interferometry

2.1 Uniqueness problem with single-wavelength interferometers

Consider the general equation for the intensity distribution from a two-beam interferometer:

$$I(x,y,k) = I_0(x,y) + I_1(x,y)\cos\left[kz(x,y) + \phi_0\right] \tag{1}$$

where x and y are two image plane coordinates, z is the optical path difference between object and reference waves, ϕ_0 is a phase shift between the waves, k is the wavenumber $2\pi/\lambda$ where λ is the wavelength, and I_0 and I_1 are respectively the dc and modulation intensities. Provided a narrow band light source such as a laser is used, Eqn. (1) is applicable to many different classes of two-beam interferometer (e.g. Michelson, Mach-Zehnder, Fizeau etc.) with either smooth or speckled wavefronts.

The usual method of analysing such interferograms is to introduce known phase shifts ϕ_0. By varying ϕ_0 over time and recording a series of interferograms, a set of equations can be written down from which the wrapped phase distribution $\phi_w = W\{kz(x,y)\}$ can be extracted, where W denotes the wrapping operator that wraps a given phase value onto the range $-\pi$ to π [1]. The true optical path difference function, $z(x, y)$, on the other hand is proportional to the *unwrapped* phase distribution ϕ_u:

$$z(x,y) = \phi_u(x,y)/k \tag{2}$$

ϕ_u is related in turn to ϕ_w as follows:

$$\phi_u(x,y) = \phi_w(x,y) + 2\pi\nu(x,y) \tag{3}$$

where $\nu(x, y)$ is an integer field variable.

The process of phase unwrapping, i.e. determining the $\nu(x, y)$ field, can be trivial for the case of optical path differences that vary smoothly with x and y. However, in many situations this is not the case. Whenever the spatial phase gradient magnitude exceeds a value of π per pixel, there may be no unique solution for $\nu(x, y)$ based on the phase data alone and phase unwrapping then becomes impossible. Even when the phase field is continuous, the unwrapped phase distribution is uncertain to a constant integral multiple of 2π. This may be termed the *uniqueness* problem of conventional interferometry at a single wavelength.

2.2 'Finite acquisition time' problem with phase shifting interferometers

A second problem is that of the *finite acquisition time* required to measure the several intensity images and perform the phase shift between them. Environmental disturbances (vibration, turbulence, etc) can cause large errors in the imposed phase shift and hence in the measured phase [2, 3]. This second problem can be effectively eliminated through the use of spatial (as opposed to temporal) phase shifting techniques and pulsed laser illumination, however the uniqueness problem still remains.

2.3 Multiple-wavelength solutions to the uniqueness problem

One partial solution to the uniqueness problem outlined in Section 2.1 is to record interferograms at two different wavelengths, λ_1 and λ_2. Whereas with single wavelength interferometry the path difference is unknown to an integral multiple of λ, with two wavelengths the path difference is unknown to an integral multiple of λ_s, the synthetic wavelength, given by

$$\lambda_s = \lambda_1 \lambda_2 / |\lambda_1 - \lambda_2| \tag{4}$$

Although this approach can improve the unambiguous path difference by an order of magnitude, at visible wavelengths this still corresponds to a sub-10 μm unambiguous optical path range. Increasing λ_s by reducing $|\lambda_1 - \lambda_2|$ amplifies the phase noise thereby increasing the risk of an unwrapping error, and therefore requires more intensity measurements to achieve sufficient signal to noise ratio. The time needed to acquire sufficient data points means that such full-field two-wavelength systems are sensitive to environmental disturbance.

Another solution involves the use of tunable laser sources in a technique called Wavelength Scanning Interferometry (WSI). A video camera is used to record sequences of interferograms at a set of discrete wavelengths [4-6]. The multiple wavelengths approach provides significantly better dynamic range than two-wavelength interferometry, but the need to record long image sequences again makes the technique vulnerable to environmental disturbance.

A third solution which forms the basis of many existing commercial absolute path length measuring instruments is the so-called Scanning White Light Interferometer (SWLI) [7-9]. In a SWLI, broad-band illumination is used to illuminate the sample. High visibility fringes are observed only in those regions of the sample where the optical path difference is close to zero. By mechanical scanning of the sample or reference mirror, the position of maximum fringe visibility is recorded on a pixel-wise basis allowing a complete path-difference map to be produced once all the points within the field of view have passed through the zero path difference surface. Once again, in addition to the need for expensive mechanical scanning devices, the main drawback is the susceptibility to environmental disturbance.

3 Hyperspectral interferometry

A new approach to the problem is proposed in this section. Although the term hyperspectral interferometry has been used on occasion in the literature, to the best of our knowledge all such references involve the use of an interferometer to determine the spectral distribution of a scene.

An image is formed by an interferometer using broad band illumination. Unlike the case of a SWLI, this 'white-light' interferogram is split optically into its constituent interferograms, each formed from a narrow spectral band within the broad spectral illumination envelope, by means of a hyperspectral imaging system. The imaging system places the narrow band images at discrete locations on a two-dimensional photodetector array (see Fig. 1). If the object is optically smooth, fringes are visible as indicated in Fig. 1 because of the narrow bandwidth of the illumination used for each frame. If the object is optically rough, a speckle field is visible rather than interference fringes, because the starting phase is random. In either case, the phase at a given pixel changes from one sub-image to the next by an amount proportional to the z value for that pixel.

After readout of the array into computer memory, the individual sub-images are registered with respect to their x and y coordinates and stacked to form a sampled hyperspectral image volume $I(x_m, y_n, k_p)$, in which the third axis specifies the wavenumber (see Fig. 2). Subscripts m, n and p take the values $m = 0,1,2,...,N_x - 1$, $n = 0,1,2,...,N_y - 1$, and $p = 0,1,2,...,N_k - 1$, respectively, where N_x, N_y and N_k are the number of sample points along the respective axes. Although not essential, it is convenient for the subsequent analysis if the sampled k values are uniformly spaced, with the k step value between successive interferograms denoted by δk.

According to Eqn. (1), the measured intensity for given location (x_m, y_n) then varies cosinusoidally with k, with angular frequency $z = z_0(x_m, y_n)$. The frequency can be

measured by performing a 1-D Fourier transform of the intensity values $I(x_m, y_n, k)$ with respect to k, after subtraction of the mean value, and searching for the peak of the transform which is located at $z = z_0(x_m, y_n)$. This process is repeated at all the (x_m, y_n) pixel locations, thereby providing absolute two-dimensional optical path difference distributions from the single shot measurement. The additional information provided by the k axis allows reliable determination of the absolute path length even though the field of view may contain spatially separated regions (e.g., R_1 and R_2 in Fig. 1), and which would therefore be impossible to unwrap correctly from a single narrow band image alone.

Expressing the approach mathematically, we first modify Eqn. (1) by incorporating an even function $w(k)$ that may be used to represent the case either of windowing the data to reduce spectral leakage, or of a non-uniform illuminating spectrum:

$$I(x_m, y_n, k) = \{I_0(x_m, y_n) + I_1(x_m, y_n)\cos[kz_0(x_m, y_n) + \phi_0]\}w(k - k_c) \qquad (5)$$

k_c is the wavenumber of the centre of the spectral band, z_0 is the optical path difference at $z = z_0(x_m, y_n)$, and the even symmetry assumption implies that $w(k) = w(-k)$.

The Fourier transform of Eqn. (5) may be calculated using the Fourier shift and convolution theorems as follows:

$$\tilde{I}(z) = \left[I_0\delta(z) + \frac{I_1}{2}\delta(z - z_0)\exp(i\phi_0) + \frac{I_1}{2}\delta(z + z_0)\exp(-i\phi_0) \right] * \left[\tilde{w}(z)\exp(-ik_c z)\right] \qquad (6)$$

where the (x_m, y_n) dependence has been dropped for clarity, where $\delta(...)$ is the Dirac delta function, and $\tilde{w}(z)$ is the Fourier transform of $w(k)$, and where * represents convolution.

Equation (6) is shown schematically in Fig. 3 after neglecting the unimportant constant phase values $\exp(\pm i\phi_0)$ and $\exp(-ik_0 z)$. A copy of $\widetilde{w}(z)$ is centred on each of the three delta functions at $z = 0$ (the dc term) and $z = \pm z_0$ (the cosine term). As a result of the even symmetry assumption, $\widetilde{w}(z)$ also possesses even symmetry and so the positions of the peaks in $\widetilde{I}(z)$ are also located at $z = 0$ and $z = \pm z_0$. Thus, finding the position of the peak in the region $z > 0$ of the function $\widetilde{I}(z)$ provides an unbiased estimator of the optical path $z = z_0$, provided the leakage of the signal from the other two peaks can be neglected. Reducing leakage from the peak centred on $z = 0$ is the main reason for removing the dc peak as outlined above.

3.1 Depth range

The maximum unambiguous depth range is given by the Shannon sampling theorem which states that in order to ensure adequate sampling of the $I(x_m, y_n, k)$ signal, the term $kz(x, y)$ in Eqn. (1) should not change by more than π between successive k samples. This leads to a maximum allowed z value of $z = z_M$ where

$$z_M = \frac{\pi}{\delta k}. \tag{7}$$

Any larger z values will be aliased onto a lower z value thus creating an under-sampling artefact.

The minimum allowed value of z, on the other hand, is $z = 0$, because the cosine function in Eqn. (1) is even. Negative z values can not therefore be distinguished from positive ones. We therefore have the allowable path difference range

$$0 \le z \le z_M. \tag{8}$$

Figure 4(a) and (b) is a schematic of the sampled $I(x_m, y_n, k)$ distribution for two z values z = 0.23z_M and z = 0.65z_M for the case N_k = 16 and a total k bandwidth Δk equal to 20% of the centre k value. The corresponding Fourier transforms $\widetilde{I}(x_m, y_n, z)$ are shown in Figs. 5(a) and (b), respectively.

3.2 Optical path resolution

The discrete Fourier transform $\widetilde{I}(x_m, y_n, z)$ contains $N_k/2$ positive frequency components, with a separation between sample points of

$$\delta z = \frac{2\pi}{N_k \delta k} . \tag{9}$$

The width of the spectral peak (i.e., distance between zero crossing points) is $2\delta z$ for the case of a uniform spectral profile of width $N_k \delta k$. If the spectrum is not uniform but rather has a non-constant profile $W(k)$, then the width of the peak is given by the width of $\widetilde{W}(k)$. In general we can write the width of the spectral peak as

$$\delta z' = \gamma \delta z . \tag{10}$$

where the constant γ takes the value 2 for a rectangular window, and 4 for a Hanning window, for example.

The precision with which z may be determined may however be much better than the value given by Eqns. (9) and (10). As shown by the vertical dotted lines in Figure 5, the Fourier transform can be interpolated to provide sub-pixel resolution, for example by zero padding the $I(x_m, y_n, k)$ vector. An efficient algorithm to find the maximum of a peak in the Fourier transform of a one-dimensional signal to sub-pixel precision was proposed

by Kaufmann et al. [10]. The ultimate factor limiting the accuracy of such an approach is the noise in the intensity signal.

4 Application to 3-D shape measurement

One application of the proposed approach is for measuring the 3-D profile of small-scale components. Currently the technique finding most favour in commercial systems is SWLI because of its ability to measure discontinuous objects unambiguously, and its excellent height resolution. However, the technique suffers from vibration artefacts due to the time to perform the scan and requires the use of expensive anti-vibration tables. As a result it is in most cases considered to be an off-line quality control tool. The short exposure time of the HSI approach proposed here on the other hand provides a potential solution to in-line quality control requirements. A previously-described interferometric profilometer proposed by Schwider and Zhou [11] also acquires data in a single shot, but only provides 1-D information (i.e. profile along a line) rather than the single-shot area scan offered by the instrument proposed here.

Figure 6 shows schematically the surface of a sample which is illuminated and observed from above. The results of section 3 can be applied to the current situation by noting that the optical path difference is twice the local distance of the sample from the surface of zero optical path difference, L. This can be written

$$z = 2\left[h_0 - h(x, y)\right], \tag{11}$$

where h_0 is the known distance from the sample datum surface to the plane of zero optical path difference, and $h(x, y)$ is the local sample height measured relative to the datum. Measurement of absolute z distributions using HSI thus provides absolute height

distributions through Eqn. (11), provided the object surface lies within the height measurement range, Δh, given by Eqns. (7) and (11) as:

$$\Delta h = \frac{z_M}{2} = \frac{\pi}{2\delta k} . \tag{12}$$

The corresponding expression for depth resolution follows from Eqns. (9) – (11) as

$$\delta h' = \gamma \delta h , \tag{13}$$

where

$$\delta h = \frac{\pi}{N_k \delta k} . \tag{14}$$

4.1 Optical system

A system to demonstrate the proof of principle of the technique is shown schematically in Fig. 7. Light from 2 sources, denoted LS_1 and LS_2, is combined by a fibre coupler, FC. LS_1 is a broadband superluminescent LED (SLED) light source (Superlum Diodes Ltd., 840 HP1) with centre wavelength 840 nm, and full width half maximum 50 nm. LS_2 is a narrowband source (He-Ne laser; wavelength 633 nm) which is useful for alignment purposes, but otherwise contributes nothing to the HSI. The output from the optical fibre passes first through an etalon, E, is next collimated by lens L_1 and then enters a Linnik interferometer head comprising beam splitter BS_1, lenses L_2 and L_3, and reference mirror RM. The sample S is mounted on a translation stage, TS, to allow the region of interest and h_0 to be adjusted.

Light from a single point P on S produces a bundle of parallel rays that enter the hyperspectral imaging system that comprises beam splitter BS_2, diffraction grating, G, and digital camera, C_1. The blazed grating is arranged in the Littrow configuration to maximize diffraction efficiency. The parallel rays are brought to a focus in the plane of the photodetector array of C_1. Without E in place, the effect of the grating is to smear the image of P along a line on C_1. The etalon, which has a specified free spectral range of 0.5 nm at 840 nm and a finesse > 15, modifies the spectral content of the illuminating beam to produce a broadband comb with uniform δk spacing, and thus produces instead a set of N_k discrete spots. Points near to P on the sample are in turn imaged onto a set of N_k neighbouring points on C_1. Thus a set of N_k images of the sample are replicated across the sensor array of camera C_1, with a wavenumber shift of δk from one image to the next. The second camera, C_2, and imaging lens L_5, are used to produce a single high-resolution broad-band image of the object to assist in alignment of the optical system. Once again, C_2 and L_5 are not an essential part of the HSI system.

The δk value for this etalon is 4.45×10^{-3} μm^{-1}. The depth range for the system is given by Eqn. (12) as 353 μm. The height resolution can be calculated from Eqns. (13) - (14) as 22.8 μm, assuming a γ value of 2 and $N_k = 62$.

The results presented in the following sections were produced from two samples: first a planar aluminized glass substrate, and secondly a stepped sample consisting of an aluminized microscope glass cover slip mounted on a planar aluminized glass substrate. An example of the intensity distribution from C_1 for the stepped sample is shown in Figure 8, in which 62 sub-images of 11×19 pixels each are formed within a horizontal band. Three such sub-images are shown magnified as in insert to Fig. 8. The step is visible as a vertical discontinuity in the fringe patterns passing approximately through the centre of the field of view. The presence of the discontinuity causes a relative shift of the fringes with changing k, which is clearly visible in these three sub-images.

4.2 Data analysis

4.2.1 Registration of the hyperspectral images

The full image of the type shown in Fig. 8 is first segmented into the individual sub-images which are then assembled to form the hyperspectral image volume $I(x_m, y_n, k_p)$, as described in the previous section. In order to perform the segmentation, the pixel coordinates of the centre of each sub-image are estimated by a two-step process. First the centre coordinates of the 1st and last sub-images are estimated manually from an image in which only the reference beam illuminates the sensor. Linear interpolation is used to provide initial estimates of the centre coordinates of all the intermediate images. These initial estimates are then refined by locally fitting a two-dimensional Gaussian function to each sub-image of the reference beam in turn. Registration in this way to the nearest pixel is sufficiently accurate for most purposes, although sub-pixel interpolation could be used if higher spatial resolution is required.

4.2.2 Background pedestal removal

Sample data from a single pixel at the centre of the field of view of the planar sample is shown in Fig. 9. Parts (a), (b) and (c) were extracted from three full hyperspectral images, each recorded at a different distance from the plane of zero optical path difference. These plots may be compared to simulated data as shown in Fig. 4; unlike the simulations, however, there is significant variation with k in both the fringe modulation and the dc offset due to the non-uniform spectrum of the SLED light source. Removal of the dc 'pedestal' may be achieved by recording separate hyperspectral image volumes of the object wave and reference waves, denoted by $I_o(x, y, k)$ and $I_r(x, y, k)$, respectively. The sums

$$s_1(x_m, y_n) = \sum_{p=0}^{N_k-1} I(x_m, y_n, k_p)$$

$$s_2(x_m, y_n) = \sum_{p=0}^{N_k-1} \left[I_o(x_m, y_n, k_p) + I_r(x_m, y_n, k_p) \right] \quad (15)$$

are the zero-frequency Fourier components of the sampled interference signal and dc pedestal, respectively. The array $I_2(x_m, y_n, k_p)$ then has the dc pedestal removed as follows:

$$I_2(x_m, y_n, k_p) = I(x_m, y_n, k_p) - (s_1 / s_2) \left[I_o(x_m, y_n, k_p) + I_r(x_m, y_n, k_p) \right] \quad (16)$$

The result of applying these equations to the signals from Fig. 9 is shown in Fig. 10.

4.2.3 Fourier transformation

Once the mean-free signal $I_2(x_m, y_n, k_p)$ has been computed according to Eqn. (16), a 1-D fast Fourier transform is applied to each pixel along the *k* axis. The peak in the magnitude of the transform is used as the starting point for the iterative sub-pixel peak search algorithm proposed by Kaufmann et al. [10]. This provides the absolute optical path length on a pixel-wise basis, from which the height distribution is calculated using Eqn. (11).

4.3 Results

4.3.1 Planar sample

Experiments were performed in which the planar sample was moved in steps of 50 μm along the optical axis of the interferometer by means of a precision translation stage. At each position a hyperspectral image volume was recorded and analysed using the

algorithm described in the previous section. The computed height at a pixel at the centre of the field of view is plotted as a function of the known location of the sample in Fig. 11. The pixel is the same one used to plot Figs. 9-10, and the position of the stage for parts (a) – (c) of those figures is shown on Fig. 11. The computed height obeys the expected 1:1 relationship with imposed location over the height measurement range, $\Delta h = 353$ μm. Once the object moves outside the range $0 < (h_0 - h) < \Delta h$, the peak in the spectrum is aliased giving rise to an erroneous position estimate. The linear response over the range $0 < (h_0 - h) < \Delta h$ is therefore modified outside this range to give a characteristic 'saw tooth' shaped response curve that is apparent in Fig. 11.

The measured height distributions of the planar sample at the three locations (a), (b) and (c) of Fig. 11 are shown in Fig. 12. The approximate noise in the measurements was estimated by fitting a plane to each of these three surfaces. The root mean square (rms) of the residual about the best fit planes was 111, 73 and 119 nm for (a) – (c) respectively, with an overall rms residual of 103 nm. A single outlier was identified in each of (a) and (c), and when these points were excluded the rms residual was reduced to 78 and 92 nm, respectively, with an overall rms for the three planes of 81 nm. This figure is higher than the values of order 1 nm (or less) typically achieved by SWLI. There are several reasons for this which may be summarized as follows. Firstly, the bandwidth of the light source actually used for the data acquisition was 30 nm which is an order of magnitude lower than that typically used in SWLI. Depth resolution scales inversely with bandwidth so one can expect a factor of 10× worse performance due to this factor alone. SLEDs with a bandwidth of 200 nm are now commercially available which should improve the performance significantly. Secondly spatial variations in photodetector sensitivity have not been taken into account so far. These variations will introduce apparent noise in the measured profiles in the case of hyperspectral interferometry, but not for SWLI, because in the latter case the same pixel provides all the data for a given point on the sample. This

effect could be significantly reduced by appropriate calibration of the image sensor, for example by determining the dark current signal and illumination sensitivity on a pixelwise basis.

4.3.2 Stepped sample

The result of analysing the interferogram of the stepped sample (Fig. 8) is shown in Fig. 13. The stepped surface that fell within the illuminated part of the sample is reproduced in the computed 3-D profile. The calculated step height of 115 μm agrees well with the true value of 120 μm.

5 Conclusions

A new interferometric approach to the problem of determining 2-D absolute optical path differences has been proposed in this paper. Unlike current methods, such as scanning white light interferometry and wavelength scanning interferometry, the data are acquired in a single shot, thereby providing significantly greater immunity from environmental disturbance. Proof of principle experiments with a 'white light' interferometer have demonstrated the applicability of the technique to the single-shot measurement of absolute 3-D profiles. An unambiguous depth measurement range of 350 μm and a depth measurement precision of approximately 80 nm (= 1 part in 4,000 of the depth range) were achieved with a bandwidth of 30 nm and a centre wavelength of 840 nm.

6 References

1. J. M. Huntley, “Automated analysis of speckle interferograms”, in “Digital speckle pattern interferometry”, ed. P. K. Rastogi, John Wiley & Sons Ltd., Chichester (2001).
2. P. de Groot, “Vibration in phase-shifting interferometry,” J. Opt. Soc. Am. A **12**, 354–365 (1995).
3. J. M. Huntley, “Suppression of phase errors from vibration in phase shifting interferometry,” J. Opt. Soc. Am. A **15** (8) 2233 – 2241 (1998).
4. S. Kuwamura and I. Yamaguchi, “Wavelength scanning profilometry for real-time surface shape measurement,” Appl. Opt. **36,** 4473–4482 (1997).
5. F. Lexer, C. K. Hitzenberger, A. F. Fercher, and M. Kulhavy, “Wavelength-tuning interferometry of intraocular distances,” Appl. Opt. **36,** 6548–6553 (1997).
6. P. de Groot, “Measurement of transparent plates with wavelength-tuned phase-shifting interferometry,” Appl. Opt. **39,** 2658–2663 (2000).
7. T. Dresel, G. Häusler, and H. Venzke, “Three-dimensional sensing of rough surfaces by coherence radar,” Appl. Opt. **31,** 919–925 (1992).
8. P. Sandoz and G,. Tribillon, “Profilometry by zero-order interference fringe identification”, J. Mod. Opt. **40** 1691-1700 (1993).
9. L. Deck and P. de Groot, “High-speed noncontact profiler based on scanning white-light interferometry”, Appl. Opt. **33** 7334-7338 (1994).
10. G. H. Kaufmann, A. Ennos, B. Gale and D. J. Pugh, “An electro-optic readout system for analysis of speckle photographs,” J. Phys. E: Sci Instrum. **13** 579-84 (1980).
11. J. Schwider and L. Zhou, “Dispersive interferometric profilometer,” Opt. Lett. **19**, 995-997 (1994).

Figure Captions

Figure 1. Portion of a hyperspectral interferometry image consisting of sub-images of the region of interest recorded with different k values. Three representative sub-images are shown from a rectangular array of sub-images centred on the black circles.

Figure 2. Hyperspectral interferometry volume $I(x, y, k)$ formed from the image shown in Fig. 1. The dotted line represents the path from which the sampled 1-D signal $I(x_m,y_n,k_p)$ ($p = 0,1,...,N_p - 1$) is extracted.

Figure 3. 1-D Fourier transform $\tilde{I}(z)$ from Eqn. (6). The signal peak of interest is located at $z = z_0$.

Figure 4. Schematic 1-D signal $I(x_m, y_n, k)$ from Fig. 2 for the two cases $z = 0.23z_M$ (top) and $z = 0.65z_M$ (bottom). Open circles indicate the sampled values $k = k_p$.

Figure 5. Fourier transform $\tilde{I}(x_m, y_n, z)$ of the two 1-D signals $I(x_m, y_n, k)$ from Fig. 4. Open circles indicate the sampled z values, and the vertical dotted lines indicate the position of the true z values used to generate the signals in Fig. 4.

Figure 6. Cross-section through sample with height distribution $h = h(x, y)$. Lines L and D are respectively cross-sections through the zero path difference and sample datum surfaces.

Figure 7. Hyperspectral interferometer for single-shot 3-D shape measurement.

Figure 8. Set of $N_k = 62$ hyperspectral images of a stepped surface spread across the horizontal axis of camera C_1. Inset: three of the hyperspectral images within the central white box enlarged by a factor 10×.

Figure 9. 1-D signal $I(x_m, y_n, k_p)$ from a pixel (x_m, y_n) close to the centre of the field of view for the planar sample at three values (increasing from (a) to (c)) of optical path difference.

Figure 10. 1-D signal from Fig. 9 after removal of the background intensity pedestal.

Figure 11. Measured position of one point on planar sample verses known sample position. Points (a) – (c) correspond to the locations of the data displayed in Figs 9 and 10.

Figure 12. Measured surface profile for the planar sample when positioned at the locations (a)-(c) of Fig. 11.

Figure 13. Surface profile of the stepped sample on a 11×19 pixel grid measured using the single-shot HSI system.

Figures

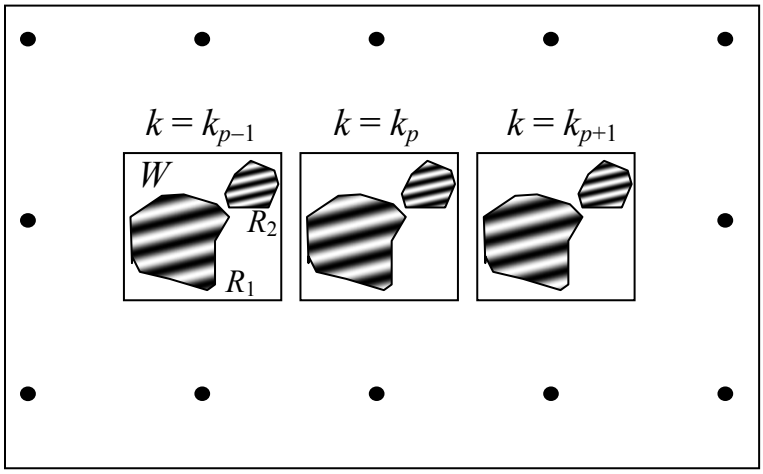

Figure 1. Portion of a hyperspectral interferometry image consisting of sub-images of the region of interest recorded with different k values. Three representative sub-images are shown from a rectangular array of sub-images centred on the black circles.

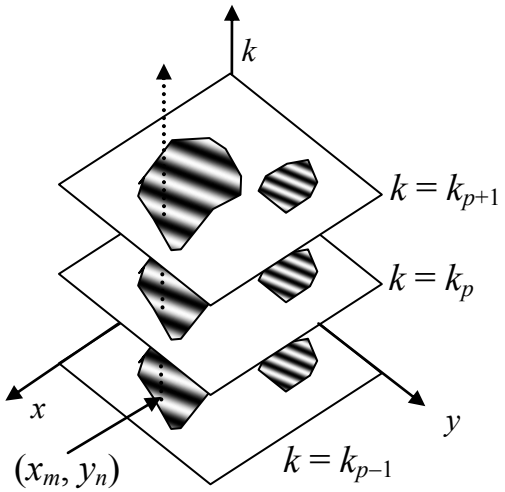

Figure 2. Hyperspectral interferometry volume $I(x, y, k)$ formed from the image shown in Fig. 1. The dotted line represents the path from which the sampled 1-D signal $I(x_m,y_n,k_p)$ ($p = 0,1,...,N_k - 1$) is extracted.

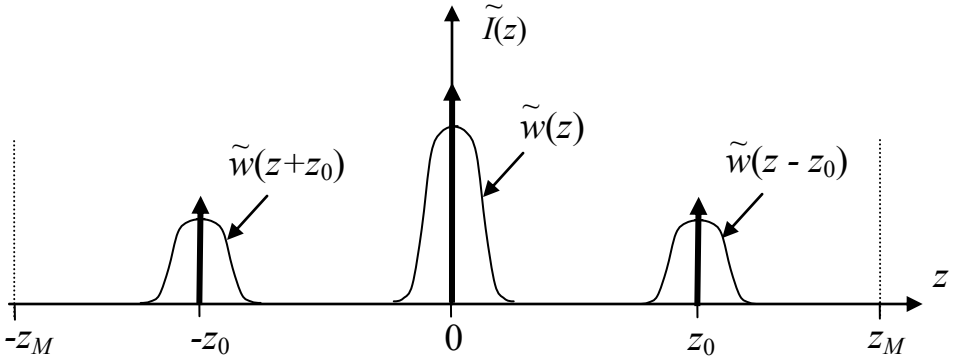

Figure 3. 1-D Fourier transform $\widetilde{I}(z)$ from Eqn. (6). The signal peak of interest is located at $z = z_0$.

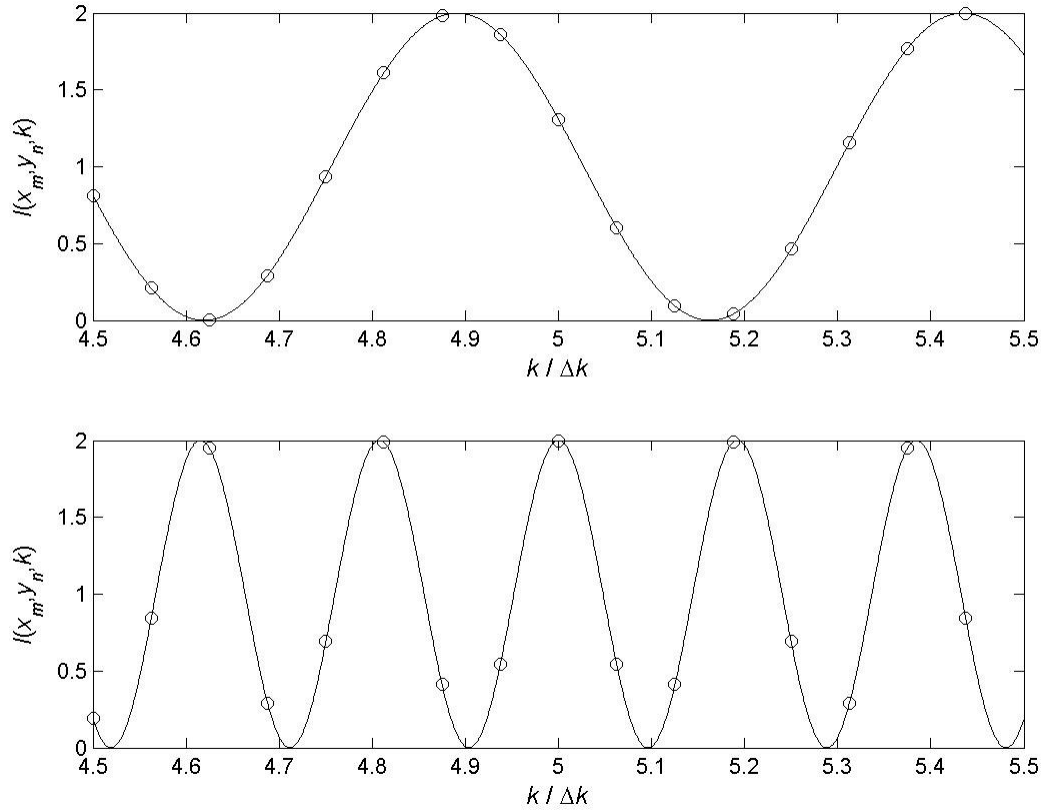

Figure 4. Schematic 1-D signal $I(x_m, y_n, k)$ from Fig. 2 for the two cases z = $0.23z_M$ (top) and $z = 0.65z_M$ (bottom). Open circles indicate the sampled values $k = k_p$.

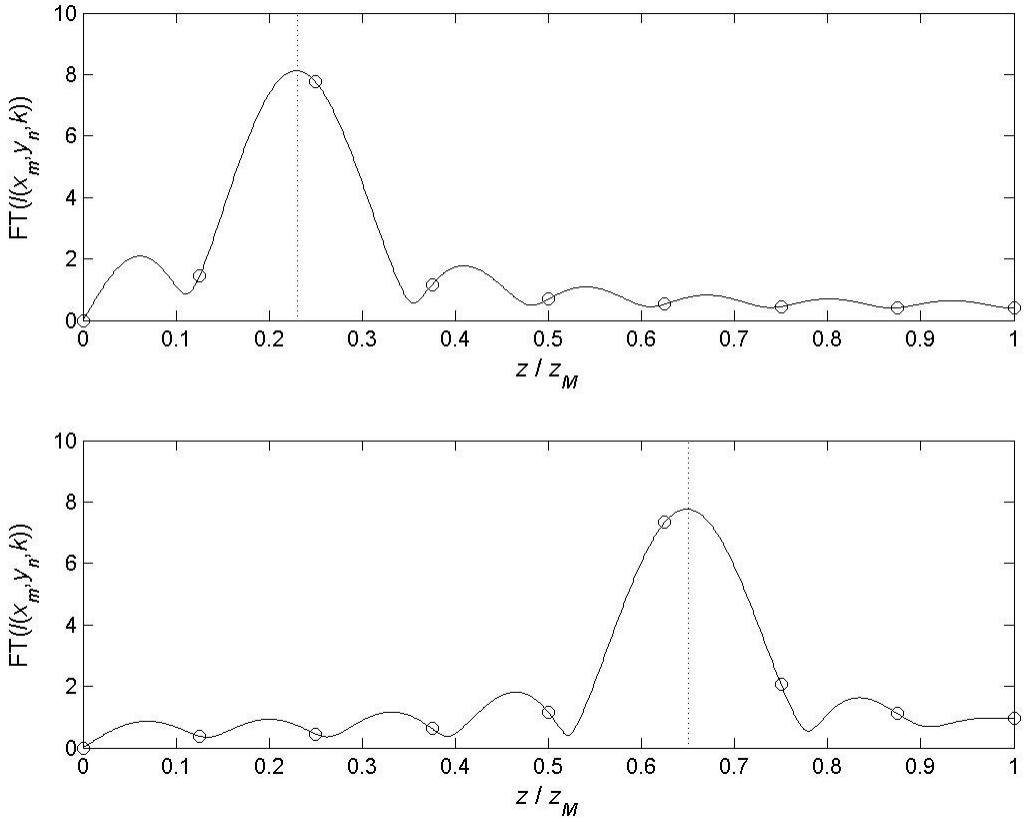

Figure 5. Fourier transform $\widetilde{I}(x_m, y_n, z)$ of the two 1-D signals $I(x_m, y_n, k)$ from Fig. 4. Open circles indicate the sampled z values, and the vertical dotted lines indicate the position of the true z values used to generate the signals in Fig. 4.

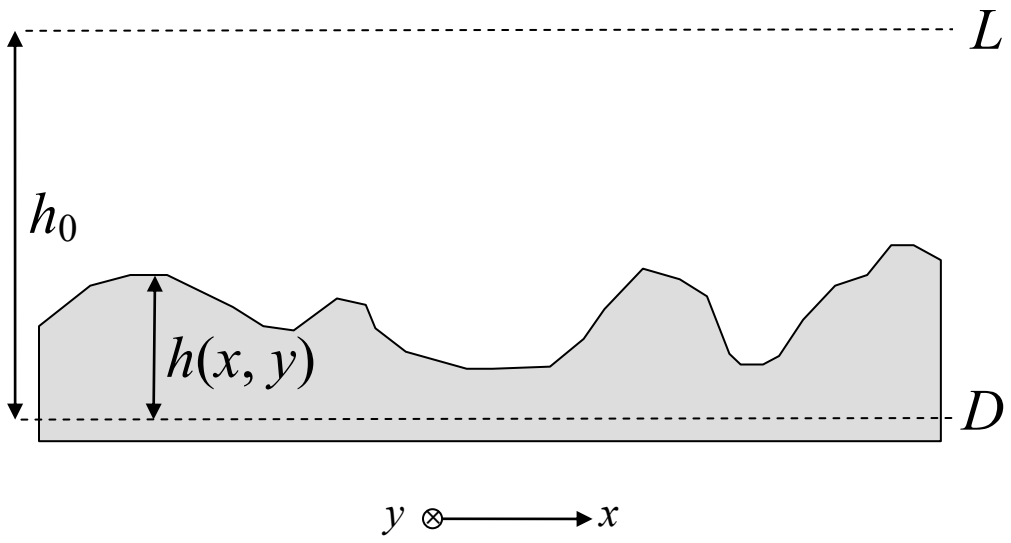

Figure 6. Cross-section through sample with height distribution $h = h(x, y)$. Lines L and D are respectively cross-sections through the zero path difference and sample datum surfaces.

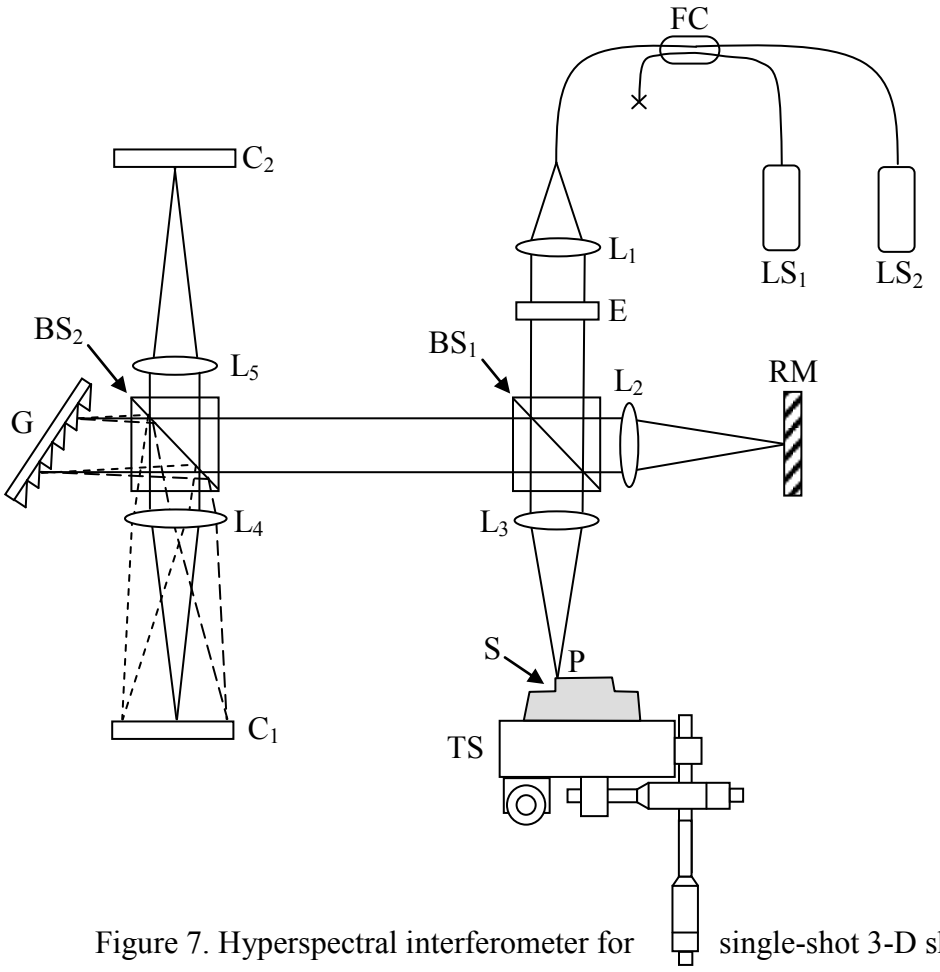

Figure 7. Hyperspectral interferometer for single-shot 3-D shape measurement.

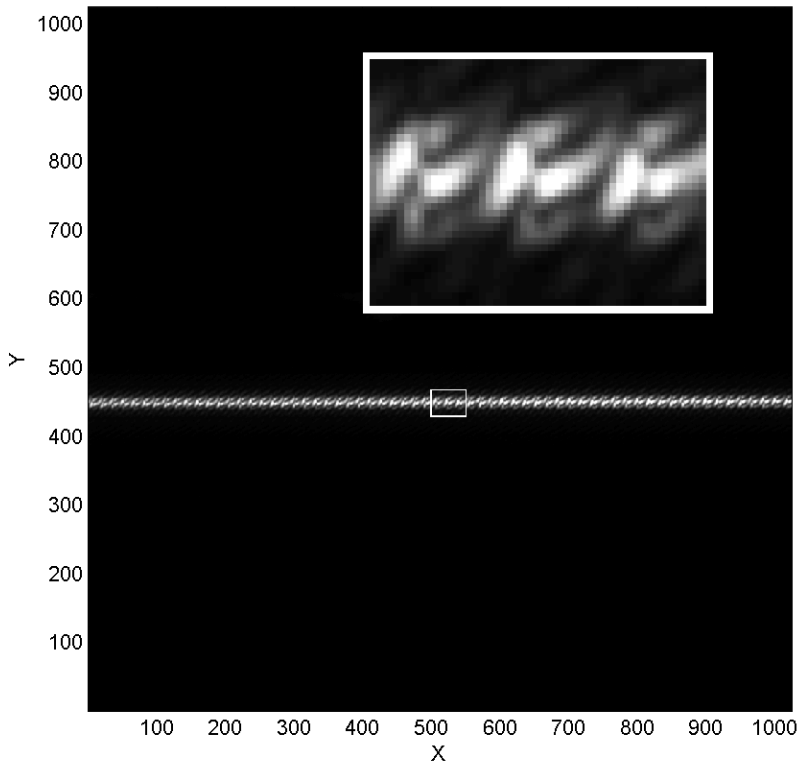

Figure 8. Set of $N_k = 62$ hyperspectral images of a stepped surface spread across the horizontal axis of camera C_1. Inset: three of the hyperspectral images within the central white box enlarged by a factor 10×.

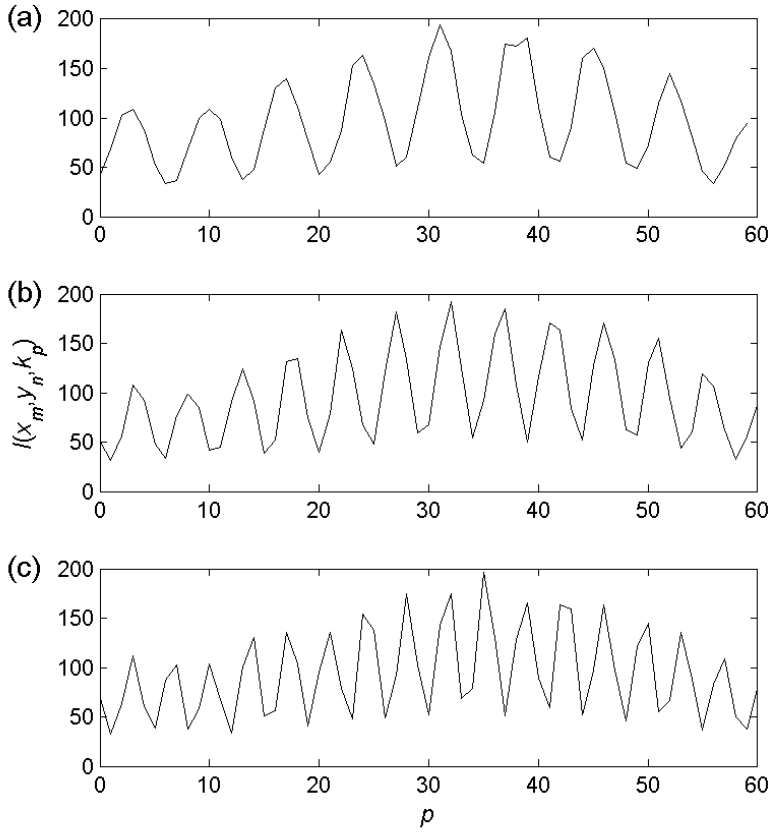

Figure 9. 1-D signal $I(x_m,y_n,k_p)$ from a pixel (x_m,y_n) close to the centre of the field of view for the planar sample at three values (increasing from (a) to (c)) of optical path difference.

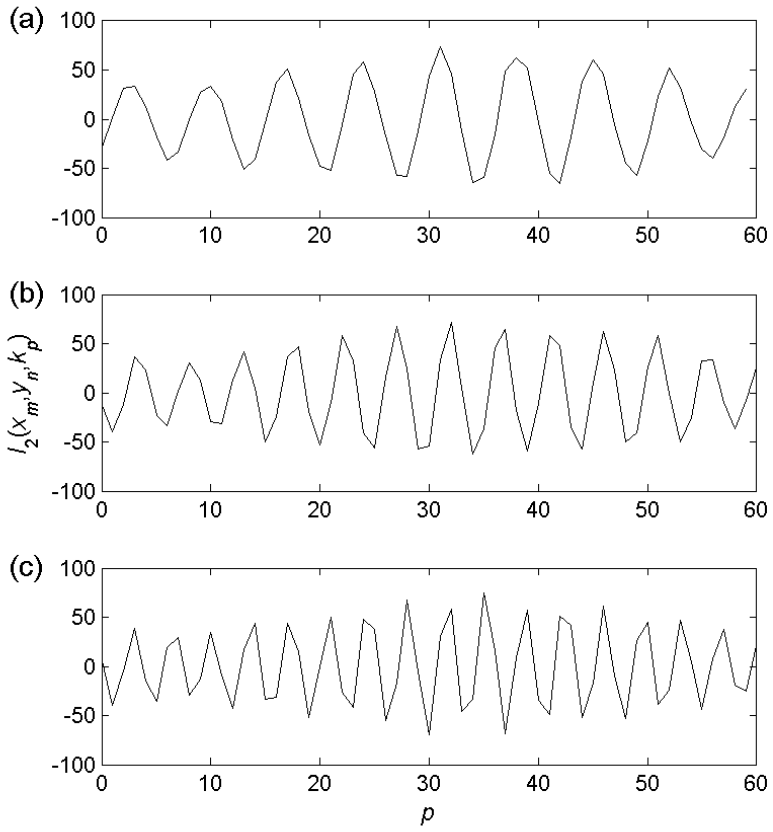

Figure 10. 1-D signal from Fig. 9 after removal of the background intensity pedestal.

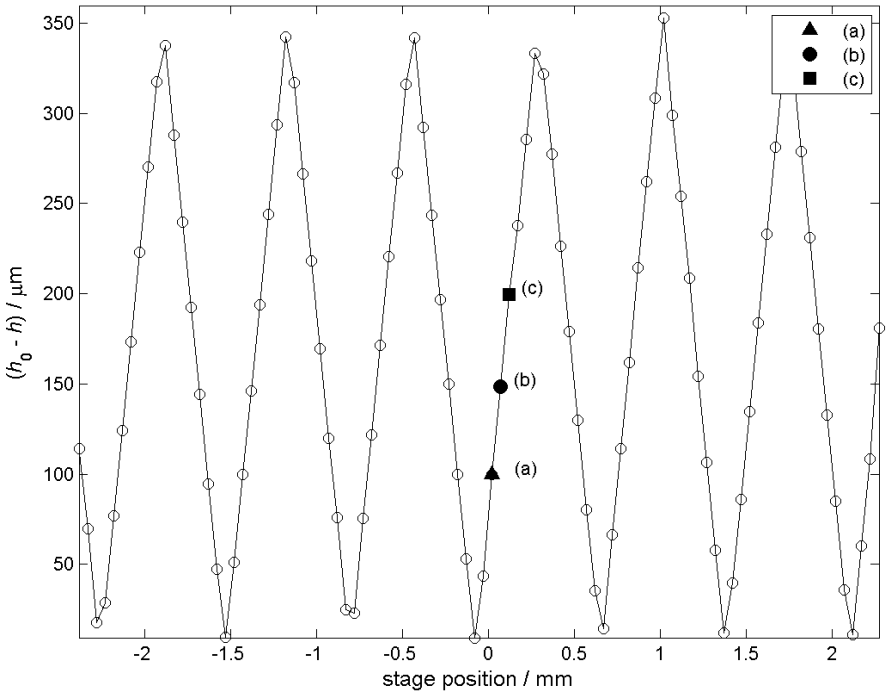

Figure 11. Measured position of one point on planar sample verses known sample position. Points (a) – (c) correspond to the locations of the data displayed in Figs 9 and 10.

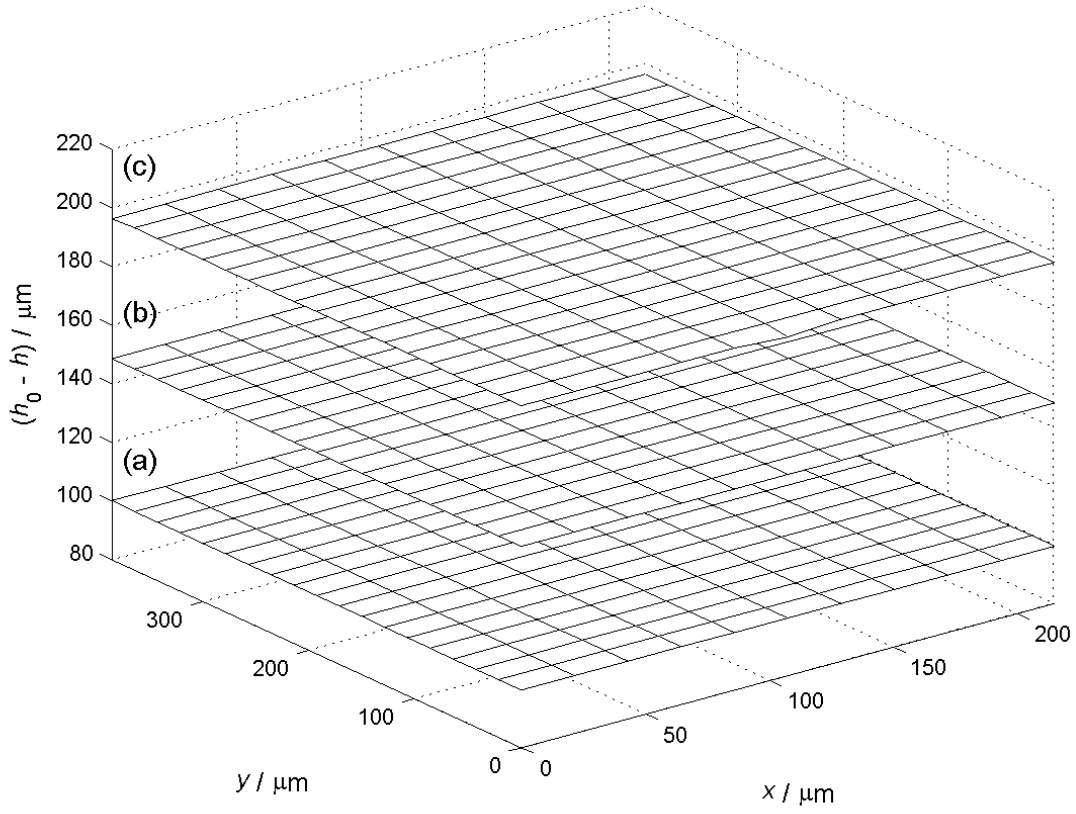

Figure 12. Measured surface profile for the planar sample when positioned at the locations (a)-(c) of Fig. 11.

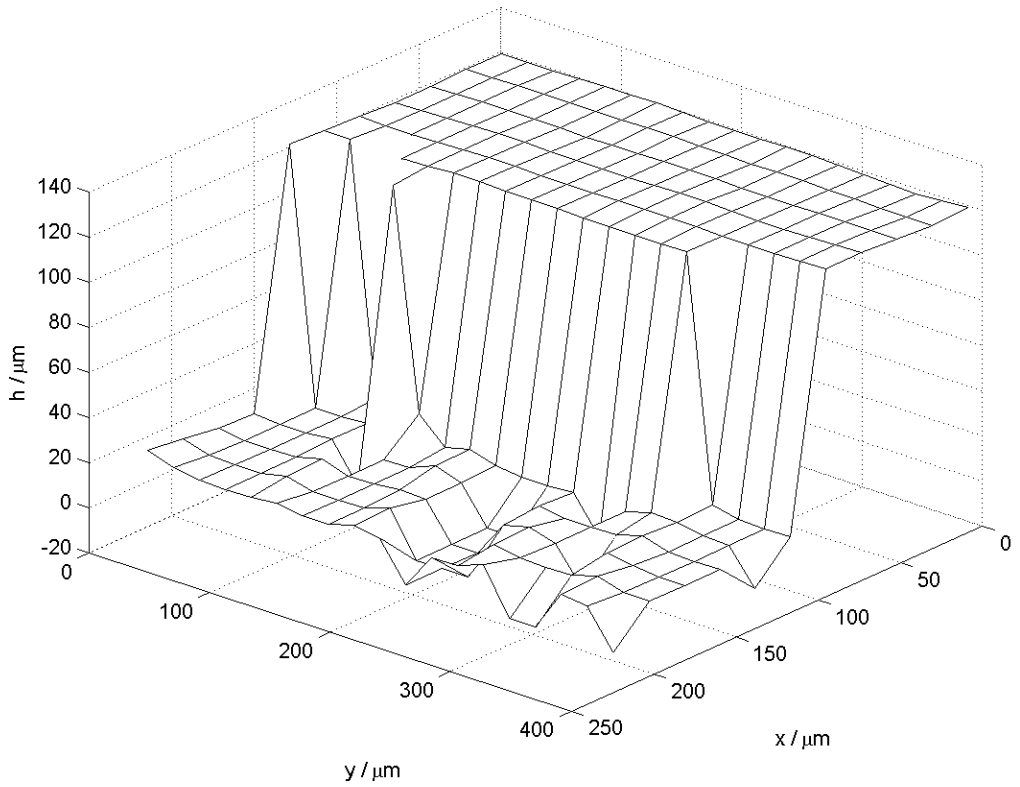

Figure 13. Surface profile of the stepped sample on a 11×19 pixel grid measured using the single-shot HSI system.